Wake Characteristics of a Submerged Underwater Vehicle in Two-layer Fluids

Gang Gao[1], Qingjie Meng[2], Liushuai Cao[1], Decheng Wan[1]*

[1] Computational Marine Hydrodynamics Lab (CMHL), School of Naval Architecture, Ocean and Civil Engineering,
Shanghai Jiao Tong University, Shanghai, China
[2] Wuhan Second Ship Design and Research Institute, Wuhan, China

[*]Corresponding Author

ABSTRACT

In ocean environment with density stratification, internal waves are generated when underwater vehicle moves. These internal waves will propagate through the water layers up to the free surface, which can be detected by Synthetic Aperture Radar (SAR). Based on the wave pattern information, the hull size, heading direction, and even the advancing velocity of the vehicle can be inferred. Previous researches have mainly focused on wave pattern characteristics, with little attention given to the features of moving vehicle wakes (Liu et al., 2020; Shi et al. 2022; Sun et al., 2023). In this paper, focus extends beyond wave pattern characteristics to encompass the alterations in wake induced by the motion of underwater vehicles. First, a comparison between experimental and numerical results is performed to verify the correctness, the large eddy simulation (LES) is used to model wake turbulence. Subsequently, a parametric study consisting of various depth to height ratios, advancing velocities and density ratios is carried out, the results indicate that when vehicle is in close proximity to the fluid interface, the wake of the moving vehicle rises rapidly and the wave pattern gradually transitions from being dominated by transverse waves to being dominated by divergent waves, with the amplitudes of both wave peaks and troughs progressively increasing. As the velocity of the moving vehicle increases, the wake exhibits a flattened and elongated characteristic. Additionally, when the density ratio between the two liquid layers decreases, the wake of the moving vehicle also rises faster.

KEY WORDS: Stratified fluid; two-layer fluids; numerical investigation; underwater vehicle wake; large eddy simulation

INTRODUCTION

Underwater navigation vehicles have long been recognized for their significant contribution to enhancing maritime combat capabilities, owing to their high concealment and formidable military strike capabilities. As the maritime situation becomes increasingly severe, there is an urgent need for effective anti-submarine missions. The key to marine anti-submarine technology lies in the ability to detect the traces of underwater vehicles and promptly determine their position, speed, and other relevant characteristics. Submarines serve as exemplary underwater vehicles, and their design, construction, and detection technologies have been evolving in parallel. Initially, sonar technology was employed as the primary anti-submarine method, relying on the reception of reflected sound waves and the detection of radiated noise to ascertain the position, size, speed, and other pertinent information of underwater vehicles. However, with the advancement of submarine technology, detecting them using traditional sonar equipment has become increasingly challenging. Consequently, non-acoustic detection technology has emerged as a research focus. When underwater vehicles navigate beneath the water's surface, they generate a distinct flow field shape on the water's surface. This interaction between the underwater vehicle and the water body leads to the formation of noticeable Kelvin waves and Bernoulli hump on the water's surface. At a certain depth, a pycnocline with significant density changes can be observed. When sailing underwater and passing through this pycnocline, the phenomenon of internal waves is induced. These internal waves propagate to the sea surface, causing convergence and divergence effects in the flow field and resulting in the formation of long-distance wakes. Synthetic aperture radar can easily detect these wakes, enabling the determination of the speed, size, and depth of the underwater vehicle. Therefore, the study of wakes and surface wave morphology of underwater vehicles in density stratification has become a focal point in the development of detection technology.

Scholars have extensively researched the mechanisms of wake generation, propagation characteristics, and water surface characteristics of underwater vehicles in density stratification. Their efforts have produced significant results. Researchers studied the turbulent wake of self-propelled objects in both uniform fluids and fluids with vertical density gradients. The findings suggest that viscosity plays a major role in the generation of internal waves (Schooley and Stewart, 1963). Researchers also focused on the generation of internal waves caused by the motion of a hemispherical model. The results clearly indicate that the Froude number has a significant impact on the formation of internal waves (Wei et al., 2011). Additionally, experiments were conducted to investigate the characteristics of internal waves excited by a dragged sphere in density stratified fluids. Intuitive expressions were derived to describe the features of steady internal waves with volume effect and unsteady internal waves with wake effect (Yao et al., 2022). Furthermore, the velocity magnitude of the internal wave flow field was determined by

analyzing its changes with the internal Froude number. To study the effects of two layers of liquids with different densities, researchers developed a horizontal towing system for an underwater vehicle. By manipulating the vehicle's movement at various water depths and speeds, they accurately measured changes in surface waves and internal waves. It was discovered that the dominance of transverse waves increases at lower velocities, while the strength of divergent waves gradually intensifies as the velocity increases. Additionally, wave pattern characteristics are influenced by the thickness and depth of the two layers of fluid with different densities (Min et al., 2023). Particle image velocimetry technology was employed in a layered flow channel to analyze the changing patterns of different waveforms, peak velocities, and Froude numbers (Sun et al., 2023).

Model experiments alone cannot provide complete information about the flow field. To further investigate the wake characteristics of underwater vehicles, computational fluid dynamics has emerged as the primary research method. Numerical simulations were conducted, yielding consistent results with experimental and theoretical findings in terms of wave pattern characteristics and wavelength (Min et al., 2023). In addition, large eddy simulation was employed to examine the surface characteristics of a moving sphere in a linear layered environment. Sun et al. (2023) pointed out that as the Froude number increases, the wake angle decreases, the wavelength increases, the surface wave amplitude increases, and the horizontal divergence moves downstream along the wake and free surface. Conversely, vertical vorticity only propagates downstream of the wake. Furthermore, a numerical simulation was performed using the $k - \varepsilon$ turbulence model and the VOF method to investigate the maneuvering motion of an underwater vehicle under different drift angles in density stratified flow. Shi et al. (2022) found that as the drift angle increases, the wake still exhibits noticeable Kelvin waveform characteristics, while the asymmetry of the surrounding flow field intensifies. Moreover, the peak and trough amplitude of the surface wave show a linear relationship with the change in drift angle. Additionally, when the drift angle remains constant, the study found that the sailing speed and diving depth significantly impact the hydrodynamic performance of the submarine. The effect of density stratification on resistance increases with higher sailing speed and greater distance from the free surface. Notably, the internal wave shape differs noticeably when sailing upward and downward along the inner interface (Liu et al., 2020). A hypothetical thermocline simulation was conducted to model a continuously stratified fluid. The VOF method was used to capture free surface waves, and the study analyzed the hydrodynamic performance, wake evolution characteristics, and free surface characteristics of underwater vehicles under different stratification strengths (Cao et al., 2023). Furthermore, an enhanced delayed separation eddy simulation modeling method was employed to accurately and efficiently solve the coherent vortex structure and turbulent wake (Cao et al., 2021).

In existing research, experimental data are insufficient to yield comprehensive flow field insights, and the numerical simulations conducted thus far have inadequately addressed the influence of multiple factors, including density ratio, velocity, and depth. Consequently, there is a need for numerical simulations under various operating conditions to undertake a comprehensive investigation. The article is structured as follows: Firstly, the numerical simulation method is described, which includes details on the computational domain, computational mesh, turbulence modeling, initial conditions, and boundary conditions. Next, numerical simulations are conducted with variations in speeds, dive depths, and stratification gradients. These simulations analyze the vortex structure, changes in the free surface, and waveform of the internal interface. Finally, conclusions are drawn based on the findings.

NUMERICAL METHODS

Governing Equation

The direct numerical simulation (DNS) method is a powerful tool for understanding turbulence and the flow evolution process. However, it requires significant computing resources. On the other hand, the Reynolds averaging (RANS) method calculates the average flow, but it neglects the turbulent pulsations that can have a negative impact on the overall flow. To address this limitation, a turbulence model is used in conjunction with the RANS method. The large eddy simulation (LES) method lies between DNS and RANS. In LES, small eddies below a certain grid size are filtered out before solving for the larger eddies. To account for the impact of the filtered small eddies on the larger ones, additional stress terms are introduced. Therefore, before establishing the filter function, all flow variables must be divided into large-scale and small-scale quantities. For any instantaneous flow variable $\bar{\varphi}(x,t)$, its large-scale quantity is defined by Equations (1) and (2).

$$\bar{\varphi}(x) = \int_D \varphi\left(x^{'}\right) G\left(x, x^{'}\right) \mathbf{d}x^{'} \tag{1}$$

$$G\left(x, x^{'}\right) = \begin{cases} 1/V & \left(x^{'} \in V\right) \\ 0 & \left(x^{'} \notin V\right) \end{cases} \tag{2}$$

x' represents the x-coordinate values of other fluid particles in the flow field. The filter function, also known as the weight function or the G function, operates on the fluid domain (D) and the volume of the computational domain control volume (V).

In the context of the Navier-Stokes equation for incompressible fluids, Large Eddy Simulation (LES) can be performed by applying a filter function to derive Equations (3) and (4).

$$\frac{\partial \boldsymbol{u}_i}{\partial x_i} = 0 \tag{3}$$

$$\frac{\partial \boldsymbol{u}_i}{\partial t} + \frac{\partial \boldsymbol{u}_i \boldsymbol{u}_j}{\partial x_j} = -\frac{1}{\rho} \frac{\partial p}{\partial x_j} + v \frac{\partial^2 \boldsymbol{u}_i}{\partial x_i x_j} - \frac{\partial \boldsymbol{\tau}_{ij}}{\partial x_j} + f_i \tag{4}$$

The velocity vectors u_i and u_j (i, j=1,2,3) are filtered to obtain their respective components in the x direction, denoted by x_i and x_j. The variables t, p, v, τ_{ij}, and f_i represent time, filtered pressure, kinematic viscosity coefficient, stress tensor at the subgrid scale, and an exogenous term, respectively. The SGS model is used for approximate analysis of the anisotropic part.

$$\tau_{ij}^a = \tau_{ij} = -\frac{2}{3} \delta_{ij} k_r \tag{5}$$

Where，δ_{ij} is the Kronecker function; k_r is the residual internal energy.

In the standard SGS model, the subgrid-scale eddy viscosity is approximated using Eqn. (6).

$$v_{\mathbf{t}} = \left(C_S \Delta\right)^2 \left|S_{ij}\right| \tag{6}$$

$$\left|S_{ij}\right| = \sqrt{2S_{ij}S_{ij}} \tag{7}$$

$$S_{ij} = \frac{1}{2}\left(\frac{\partial u_i}{\partial x_j} + \frac{\partial u_j}{\partial x_i}\right) \tag{8}$$

In this study, use C_S to represent the Smagorinsky constant, which has a fixed value of 0.1. Δ is used to denote the filter size, with grid unit sizes being equal. $|S_{ij}|$ represents the rate at which the strain decomposition speed decreases after filtering. The viscosity is then employed to calculate the anisotropic subgrid stress tensor, as shown in Eqn.(9).

$$\tau_{ij}^a = -2v_t \overline{S_{ij}} \tag{9}$$

The Volume of Fluid (VOF) method is used to simulate the flow of fluid on the free surface and interface. The α_n value represents the volume fraction of the nth fluid: $\alpha_n=0$ indicates an empty state, $\alpha_n=1$ indicates the fluid is completely filled, and $0<\alpha_n<1$ represents a partial filling of the nth type of fluid. The fluids can mix with each other. The volume fraction should satisfy Eq. (10), which means that the sum of volume fractions of all grid cells must be equal to 1.

$$\sum_{n=1}^{N} \alpha_n = 1 \tag{10}$$

here, N represents the number of fluids, and in this article, $N=3$ (air, oil, water).

SOLVERS SETUP

Geometric Model and Simulation Setup

The calculation domain is shown in Figure 1. The length of the underwater vehicle is represented by L. The left and right sides of the calculation domain are positioned 5L away from the axis of the underwater vehicle. The front of the calculation domain is located 22L from the head of the underwater vehicle. The thickness of the two fluids is denoted as h_1 and h_2, respectively. The distance from the axis of the underwater vehicle body to the free surface is denoted as h. The densities of the two fluids are represented by ρ_1 and ρ_2, respectively. The specific shape and dimensions of the underwater vehicle are illustrated in Figure 2. The geometric model utilized for calculations comprises three main components: a hemispherical head, a cylindrical middle section, and a semi-ellipsoidal tail. The radius of the hemisphere matches the radius of the cylinder, with the cylinder's radius being equivalent to the maximum radius of the semi-ellipsoid. Specifically, the hemisphere has a radius of 1 cm, while the lengths of the cylinder and semi-ellipsoid are 4 cm and 5 cm respectively. The total length of the model, spanning from the hemisphere's starting point to the semi-ellipsoid's end point, defines the overall length of the model at 10 cm.
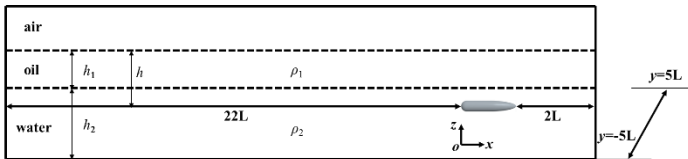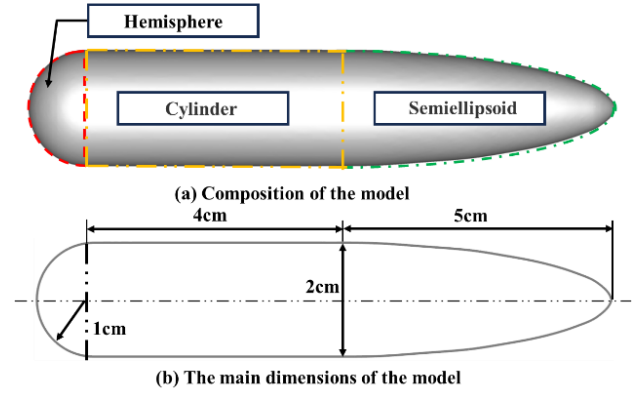

Fig. 1. Computational domain

Fig. 2. Geometric model (Min et al., 2023)

Grid Generation

As shown in Figure 3, in terms of grid division, since the self-propulsion method is used to carry out numerical simulation, local grid refinement is performed in the movement area of the sailing body, and local grid refinement is performed on the fluid interface of the air-oil and oil-water layers. The number of grids in the entire computational domain is 22 million.
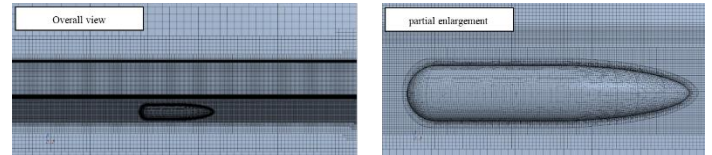

Fig. 3. Computational mesh

Boundary Setting and Discretization Format

The boundary conditions for the calculation domain are as follows: the front, left, and right sides, as well as the upper and lower boundaries, are set as velocity inlet conditions. The boundary conditions behind the underwater vehicle are set as pressure outlet conditions. Furthermore, the surface of the underwater vehicle is set as a wall boundary condition.

Condition Setting

There are two modes of fluctuations in a two-layer fluid: surface waves and internal waves. Each mode corresponds to a critical Froude number, Fr_1 and Fr_2, respectively. The expressions for these modes are as follows:

$$Fr_n^2 = \frac{1}{2} + (-1)^{n+1}\sqrt{\frac{1}{4} - \frac{(1-\gamma)h_1 h_2}{(h_1+h_2)^2}} \tag{11}$$

γ, h_1, and h_2 represent the density ratio between the upper and lower fluid layers and the depth of the upper and lower fluid layers, respectively. The subscripts $n=1$ and $n=2$ represent the surface wave and internal wave modes, respectively.

The Froude number based on the total depth is defined as follows:

$$Fr = \frac{U}{\sqrt{g(h_1+h_2)}} \tag{12}$$

When $Fr_2 < Fr < Fr_1$, the surface wave mode consists of both transverse and divergent waves, while the internal wave mode only consists of divergent waves. Table 1 presents the calculated parameters. The first to fourth working conditions primarily analyze the influence of motion speed on wake flow, while the fifth to seventh working conditions focus on the influence of diving depth position on wake flow. The eighth to tenth operating conditions primarily examine the impact of the density ratio of the two layers on the wake.

Table 1. Computational cases

Case	h_1(m)	h(m)	ρ_1(kg.m^{-3})	$\gamma = \rho_1/\rho_2$	Fr_1	Fr_2	Fr
1	0.05	0.07	917.00	0.92	0.981	0.019	0.221
2	0.05	0.07	917.00	0.92	0.981	0.019	0.443
3	0.05	0.07	917.00	0.92	0.981	0.019	0.664
4	0.05	0.07	917.00	0.92	0.981	0.019	0.886
5	0.05	0.02	917.00	0.92	0.981	0.019	0.443
6	0.05	0.03	917.00	0.92	0.981	0.019	0.443
7	0.05	0.09	917.00	0.92	0.981	0.019	0.443
8	0.05	0.07	917.00	0.90	0.976	0.024	0.443
9	0.05	0.07	917.00	0.94	0.986	0.014	0.443
10	0.05	0.07	917.00	1.00	1.000	0.000	0.443

To validate the accuracy of the calculation method, a numerical simulation is conducted to study the movement of an underwater vehicle in two layers of fluid. The obtained results are then compared with the experimental findings mentioned in Reference (Min et al., 2023). The simulation is carried out under Case B-2 working condition, using the same parameters and calculation domain settings as the test. Figure 4 illustrates the calculation and test results of wave height along the center line of the free surface. It can be observed that although there is a significant discrepancy between the numerical simulation and test results at a certain distance from the $x=0$ position, overall, the results obtained from the simulation align well with the experimental findings.
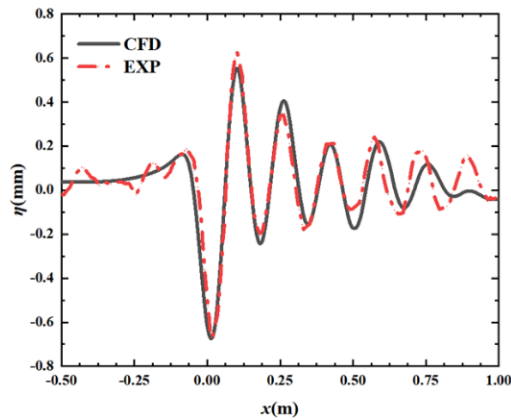

Fig. 4. Wave profiles of the free surface at $y = 0$ (Min et al., 2023)

RESULTS AND DISCUSSION

Influence of underwater vehicle advancing speed

The internal interface wave height nephogram of an underwater vehicle at different moving speeds is presented in Figure 5. When the total thickness of the fluid and the depth position of the underwater vehicle remain constant, a larger Froude number indicates a higher speed of the vehicle. It can be observed from Figure 5 that as the speed increases, the waveform angle of the internal wave decreases. Figure 6 illustrates the free surface wave height nephograms at different moving speeds of the underwater vehicle. With increasing speed, the transverse waves characteristics become more prominent. Moreover, as the speed further increases, the divergent waves strengthen and the waveform angle decreases. Additionally, the Bernoulli hump directly above the underwater vehicle gradually increases in size.
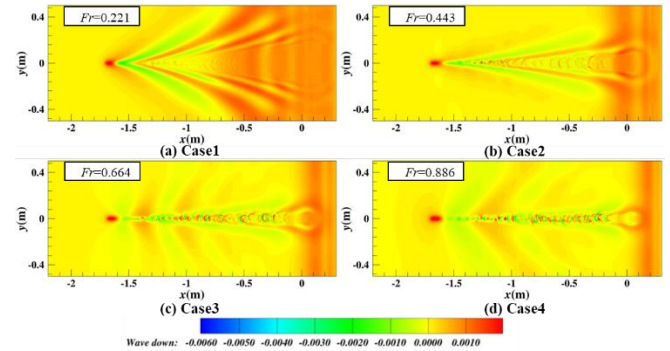

Fig. 5. Distribution of waves on the internal surface with different motion speeds.
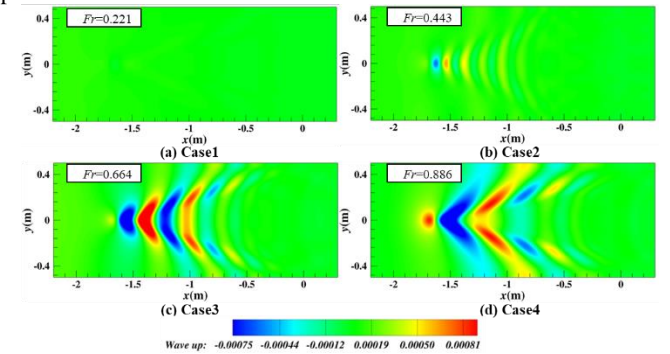

Fig. 6. Distribution of waves on the free surface with different motion speeds.
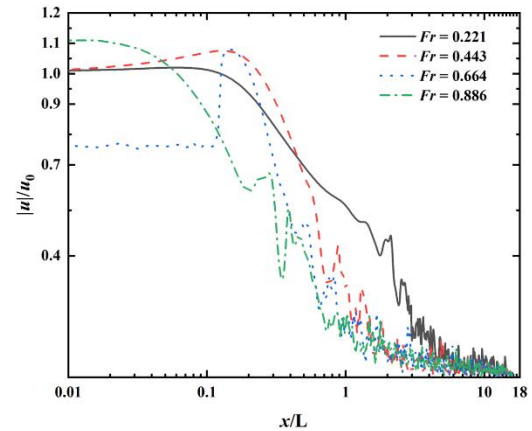

Fig. 7. Speed ratio change curve at the axis position of the underwater vehicle with different motion speeds.

The local velocity at the body axis position is determined by considering the underwater vehicle's tail as the origin of the coordinates and the direction from the bow to the tail as the positive direction. The ratio of the absolute value of the local velocity to the underwater navigation body's own motion speed can be obtained, as shown in Figure 7. The first stage of $0.01 < x/L < 0.2$, the ratio is greater than 1, it indicates the generation of turbulent flow. As the ratio reaches its peak, begins to decay,

sharply becoming smaller and finally vibrating within a certain range. In the decay stage of the ratio, the working condition with a larger Froude number decays faster.

Figure 8 illustrates the variations in the vortex structure of an underwater vehicle at different Froude numbers. As the Froude number increases, the turbulent flow becomes more drastic, leading to significant changes in the vortex structure at the stern and a shift in the position where the wake vortex shedding. In Figure 9, the graph shows the change in free surface wave height. It reveals that as the Froude number increases, the underwater vehicle's head position at x=-1.7m experiences a higher Bernoulli hump nearby. Moreover, the wavelength, period, peak, and trough values of the surface wave also increase with the Froude number. Figure 10 displays the change curves of internal interface wave heights under different Froude numbers. As the speed of the underwater vehicle increases, the peak value of the internal wave gradually becomes larger, and the trough position of the internal wave moves farther away from the vehicle's stern.

(a) Case1

(b) Case2

(c) Case3

(d) Case4
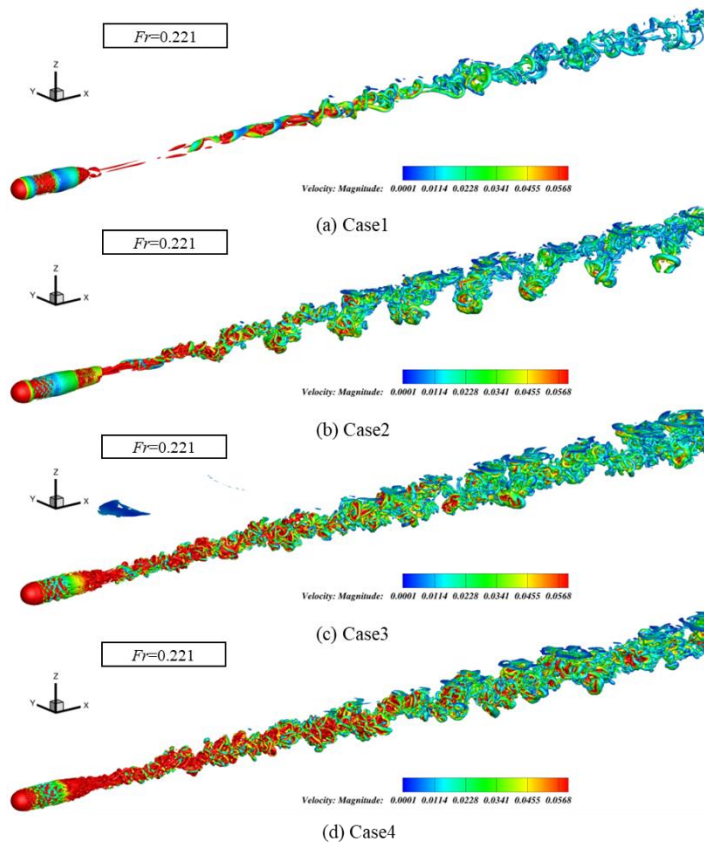
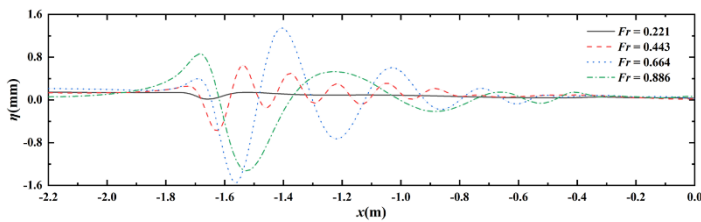Fig. 8. Isosurfaces of Q level, colored by the magnitude of velocity

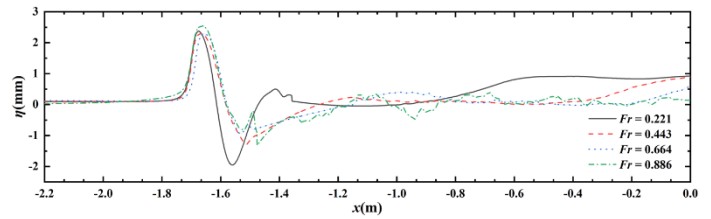Fig. 9. Wave profiles of the free surface at $y = 0$ at different motion speeds.

Fig. 10. Wave profiles of the inner surface at $y = 0$ at different motion speeds.

Influence of submerged position

The underwater vehicle is positioned above the inner interface of the two fluid layers when the diving depth is at h=0.02m and h=0.03m, with h=0.03m being closer to the inner interface. Conversely, when the diving depth is at h=0.07m and h=0.09m, the vehicle is positioned below the inner interface, with h=0.07m being closer to the inner interface. Figure 11 depicts the nephogram of wave heights at the internal interface for different positions of the underwater vehicle.

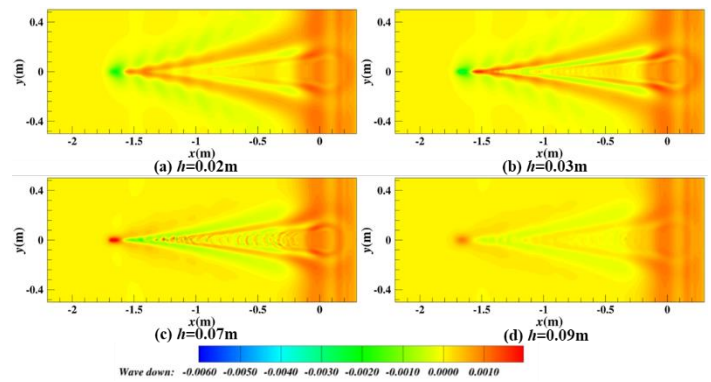(a) h=0.02m

(b) h=0.03m

(c) h=0.07m

(d) h=0.09m

Fig. 11. Distribution of waves on the internal surface with different submerged depths.

Figure 12 illustrates the wave height nephogram of the free surface at various positions of the underwater vehicle. As the distance decreases, the transverse waves characteristics gradually increase. Moreover, the divergent waves become more apparent and the waveform angle gradually decreases. Additionally, both the peak and trough values increase.

(a) h=0.02m
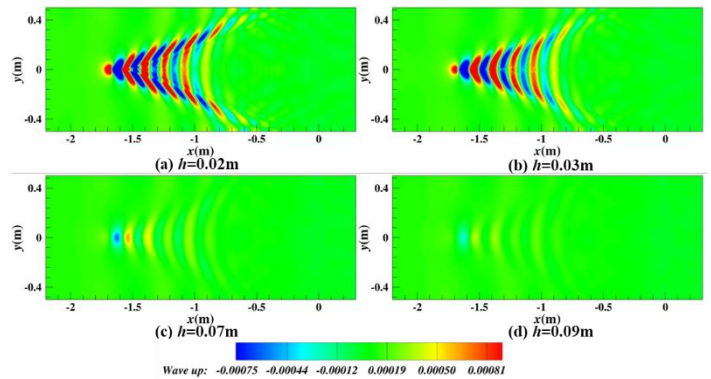
(b) h=0.03m

(c) h=0.07m

(d) h=0.09m

Fig. 12. Distribution of waves on the free surface with different submerged depths.

Same as the previous section, select the local velocity at the axis position of the underwater vehicle to get the ratio of the absolute value of the local

velocity to the underwater vehicle's own motion speed. As shown in Figure 13. By comparing the curves at different depths, it is observed that as the distance from the free surface decreases, the curve attenuates more rapidly. At $h=0.02$m and $h=0.03$m, the ratio at x/L=0.01 is approximately equal to 1, suggesting that the wake generated after launching the vehicle at these depths does not result in significant turbulent flow.
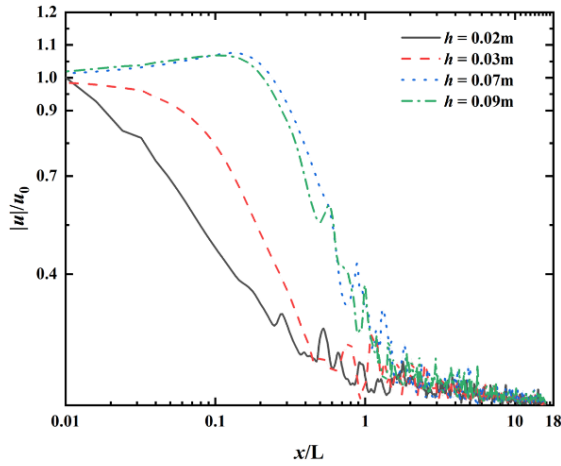

Fig. 13. Speed ratio change curve at the axis position of the underwater vehicle with different submerged depths.

Comparing the curves of free surface wave height change at different positions, as shown in Figure 14, it is evident that the surface wave crests and troughs caused by the motion of the underwater vehicle become more pronounced when $h=0.02$m and $h=0.03$m. This is because the underwater vehicle is closer to the free surface at these positions, resulting in slightly smaller wavelengths and periods of the waves. Furthermore, Figure 15 demonstrates that the wave height change curves above and below the inner interface exhibit opposite phases for all four working conditions. It can be observed that the proximity of the inner interface to $h=0.03$m and $h=0.07$m leads to higher wave height and trough values at the inner interface.
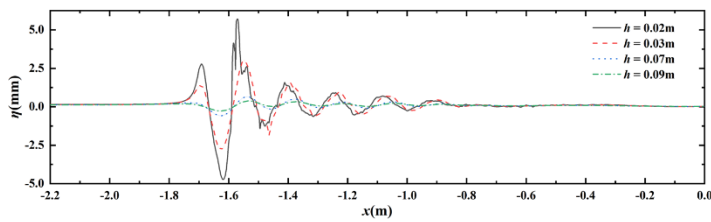

Fig. 14. Wave profiles in the free surface at $y = 0$ with different submerged depths.
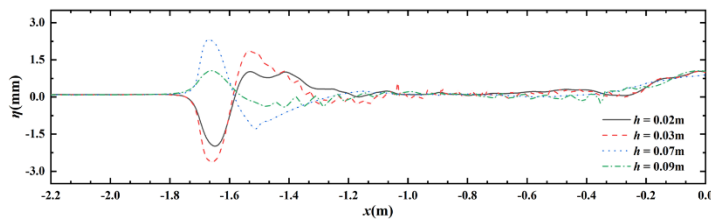

Fig. 15. Wave profiles in the internal surface at $y = 0$ with different submerged depths.

Influence of the density of the stratified fluid

Figure 16 presents a diagram depicting the wave height nephogram of the internal interface under three different density ratios of two fluid layers. The diagram illustrates that as the density ratio of the two fluid layers increases, indicating a closer similarity in their densities, the waveform angle of the internal interface wave height nephogram decreases. Combined with the previous section, when the movement speed is lower, the waveform angle of the internal interface wave height nephogram is larger, this implies that a larger difference in density between the two fluid layers results in a greater obstruction to the movement of underwater vehicles. In Figure 17, the free surface wave height nephograms are compared for four different density ratios of two-layer fluids. The Bernoulli hump near the bow of the underwater vehicle exhibits slight changes, while the free surface waveform remains mostly unchanged. Further analysis of wave height variations is required to explore the impact of the density ratio of the two fluid layers on surface waves.

Figures 18 and 19 depict the variations in wave height for surface waves and internal waves at different density ratios of the two fluid layers. As the density difference between the two fluid layers increases, the ratio becomes smaller, the peak and trough values of the surface wave also increase. The density ratios chosen for this study are relatively close, resulting in similar changes in wavelength and period of the free surface wave height curve. In contrast, the internal wave height change curve shows that the peak values of the waves remain mostly similar under different conditions of density ratios in the two fluid layers, while the size and location of the trough values exhibit slight variations.
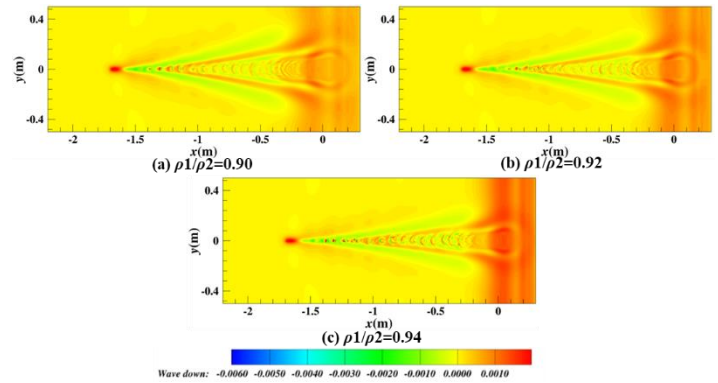

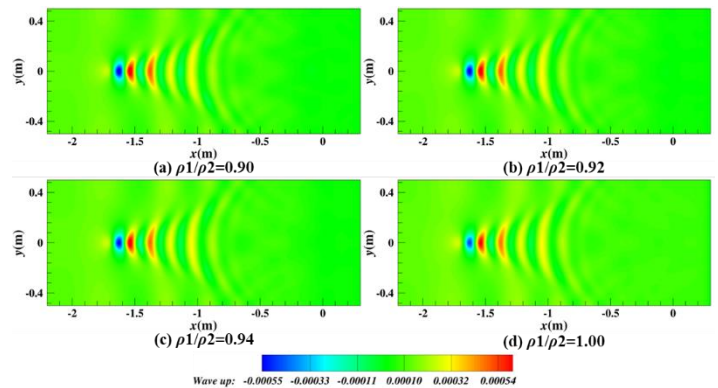Fig. 16. Distribution of waves on the internal surface with different density ratios.

Fig. 17. Distribution of waves on the free surface with different density ratios.
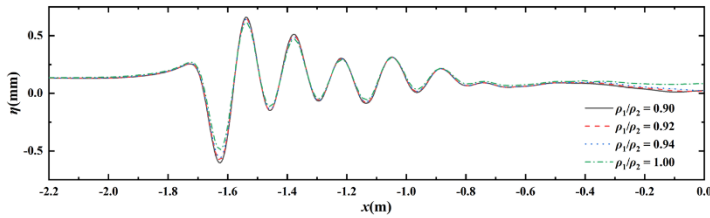
Fig. 18. Wave profiles of the free surface at $y = 0$ at different density ratios.
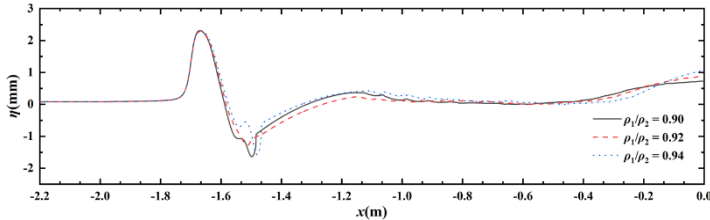

Fig. 19. Wave profiles of the inner surface at $y = 0$ at different density ratios.

Similarly, the local velocities at different distances along the axis of the underwater vehicle were analyzed to determine the ratio of the absolute value of the local velocity to the underwater vehicle's own motion speed. In Figure 20, the change curves under different two-layer fluid density ratios are compared. It can be observed that the output curve can be divided into three sections: the 'rising section', the 'attenuation section', and the 'oscillation section'. Since the ratio of the fluid densities of the two layers is very close, the values of the four change curves are also very similar. Where $x/L < 0.2$, all four change curves have values greater than 1, indicating the occurrence of turbulent flow. As the density ratio of the two fluid layers decreases, the value of the curve increases. Where $0.4 < x/L < 0.7$, as the density ratio of the two fluid layers increases, the value of the curve decreases, indicating suppression of the wake.
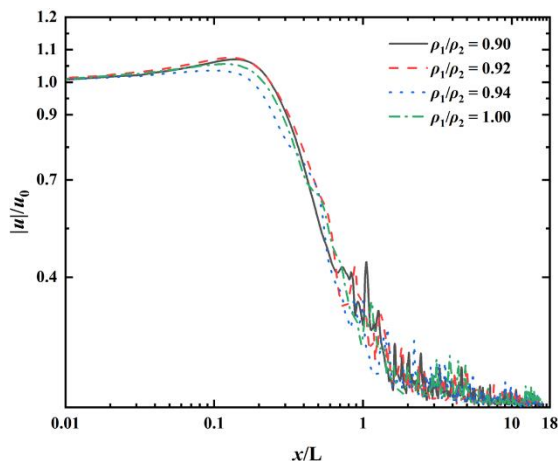

Fig. 20. Speed ratio change curve at the axis position of the underwater vehicle with different density ratios.

CONCLUSIONS

In this article, a numerical simulation of the motion of an underwater vehicle in two layers of fluid is conducted using the large eddy simulation method and the VOF method. The study investigates the effects of the underwater vehicle's motion speed, diving depth position, and the density ratio of the two layers of fluid on the surface waves and internal waves. The study examines the wave height change curves of surface waves and

internal waves, and compare the changes in the wake vortex structure of the underwater navigation body.

(a) As the speed increases, the angle of the internal wave waveform decreases. With an increase in the Froude number, more intense turbulent flow occurs, and the vortex structure at the stern undergoes significant changes. The location of vortex shedding also moves further away. Furthermore, the wavelength and period of the surface wave increase, along with the amplitude of the wave's peak and trough values.

(b) The position of the underwater vehicle has a significant impact on internal waves, particularly when it is closer to the inner interface between the two layers of fluid. When the vehicle is closer to the free surface, the characteristics of surface waves become more pronounced. The vehicle's location above and below the inner interface leads to opposite changes in the phase of the internal wave height curve. Additionally, being closer to the free surface results in greater suppression of turbulent flow around the underwater vehicle's axis.

(c) As the density difference between the two layers of fluid increases, the resistance to the movement of the sailing vehicle intensifies. This leads to an increase in the angle of the internal wave and the amplitude of the surface wave, with larger peaks and troughs. As the density difference between the two layers of fluid increases, the wake turbulent flow at the vehicle axis position is further suppressed.

REFERENCES

Cao, L. S., Gao, G., Guo, E. K., & Wan, D. C. (2023). Hydrodynamic performances and wakes induced by a generic submarine operating near the free surface in continuously stratified fluid. *Journal of Hydrodynamics*, 35(3), 396-406.

Cao, L. S., Huang, F. L., Liu, C., & Wan, D. C. (2021). Vortical structures and wakes of a sphere in homogeneous and density stratified fluid. *Journal of Hydrodynamics*, 33(2), 207-215.

Liu, S., He, G., Wang, Z., Luan, Z., Zhang, Z., Wang, W., & Gao, Y. (2020). Resistance and flow field of a submarine in a density stratified fluid. *Ocean Engineering*, 217, 107934.

Min, E. H., Heo, S., Yang, H., Lee, J. H., Koo, W., Paik, K. J., ... & Kim, H. R. (2023). Experimental and numerical study on wave characteristics by a moving submerged body in a two-layer fluid. *Ocean Engineering*, 281, 114979.

Schooley, A. H., & Stewart, R. W. (1963). Experiments with a self-propelled body submerged in a fluid with a vertical density gradient. *Journal of Fluid Mechanics*, 15(1), 83-96.

Shi, C., Cheng, X., Liu, Z., Han, K., Liu, P., & Jiang, L. (2022). Numerical Simulation of the Maneuvering Motion Wake of an Underwater Vehicle in Stratified Fluid. *Journal of Marine Science and Engineering*, 10(11), 1672.

Sun, J., Wang, Z., Chai, J., Wang, Z., & Yang, Z. (2023). Characteristics of the surface signatures induced by a sphere in a linearly stratified flow. *Ocean Engineering*, 287, 115818.

Wei, G., Wu, N., Xu, X. H., Su, X. B., & You, Y. X. (2011). Experiments on the generation of internal waves by a hemispheroid in a linearly stratified fluid. *Acta Physica Sinica -Chinese Edition-*, 60(4).

Yao, Z. C., Zhang, J., Gao, D. B., Liu, C. Q., & Hong, F. W. (2022). Experiment on surface wake of internal waves generated by underwater vehicle in stratified fluids. *Journal of Hydrodynamics*, 34(2), 277-285.